Ice Modeling Indicates Formation Mechanisms of Large-scale Folding in Greenland's Ice Sheet

Yu Zhang[1], Till Sachau[1], Steven Franke[1,2], Haibin Yang[3], Dian Li[1,4], Ilka Weikusat[1,2], and Paul D. Bons[1,5]

[1]Department of Geosciences, Tübingen University, Tübingen, Germany.

[2]Alfred Wegener Institute, Helmholtz Centre for Polar and Marine Research, Bremerhaven, Germany.

[3]School of Earth Sciences, Zhejiang University, Hangzhou, China.

[4]College of Earth Science, Chengdu University of Technology, Chengdu, China.

[5]School of Earth Science and Resources, China University of Geosciences (Beijing), Beijing, China.

Corresponding author: Y. Zhang (yu.zhang@mnf.uni-tuebingen.de), P. D. Bons (paul.bons@uni-tuebingen.de)

Key Points:

- The formation of large-scale folds in polar ice sheets is controlled by ice anisotropy and bedrock topography
- Ice anisotropy can also produce small-scale folds of originally flat ice layers
- The implementation of ice anisotropy should be included in large-scale ice flow modeling

Abstract

Radio-echo sounding (RES) has shown that large-scale folds in the englacial stratigraphy is ubiquitous in Greenland's ice sheet. However, there is no consensus yet on how these folds form. Here, we use the full-Stokes code Underworld2 to simulate ice movements in three-dimensional convergent flow, mainly investigating the effect of ice anisotropy due to a crystallographic preferred orientation, vertical viscosity and density contrasts in ice layers, and bedrock topography. Our simulated folds show complex patterns and are classified into three types: large-scale folds, small-scale folds and basal-shear folds. The amplitudes of large-scale folds tend to be at their maximum in middle ice layers and decrease towards the surface, in accordance with observations in RES data. We conclude that bedrock topography contributes to perturbations in ice layers, and that ice anisotropy amplifies these into large-scale folds, while vertical viscosity contrasts in ice layers are insufficient for large-scale fold amplification.

Plain Language Summary

Polar ice sheets are composed of compacted former snow layers that have been deposited at the ice surface. If not distorted or deformed, these layers are flat or adapt to the underlying bed topography. However, vertical radar scans of the Greenland ice sheet show large-scale folds of up to hundreds of meters in height. To investigate how these large-scale folds form, we set up a three-dimensional numerical ice-sheet model and simulate fold growth. Our modeling emphasizes the distinctive physical properties of ice required for fold formation, notably its anisotropy (the direction dependency of the flow strength) and power-law rheology (when ice becomes softer with increasing strain rate). These findings may introduce novel perspectives to the glaciological community regarding the dynamics of ice flow. For instance, the power-law behavior of ice could potentially be influenced by anisotropy and bottom shearing during flow. This suggests that ice sheets might exhibit increased instability when set in motion, raising important concerns within the field of glaciology.

1 Introduction

Airborne radio-echo sounding (RES) data reveal internal layering and large-scale folding (up to > 100 m fold amplitude) on the bumpy bedrock in several regions of the Greenland Ice Sheet (GrIS, Figure 1) (Bell et al., 2014; Bons et al., 2016; Franke et al., 2022a, 2022b; Leysinger-Vieli et al., 2018; MacGregor et al., 2015; NEEM community members, 2013; Wolovick et al., 2014). The large-scale folds appear both within ice streams and in regions of slow-moving ice. Fold amplitudes usually reach their maximum in the middle layers, gradually decrease towards upper layers and flatten at the ice surface. These folds play a significant role in the interpretation of the stratigraphy in ice cores (NEEM community members, 2013), the past and present ice flow dynamics (Franke et al., 2022a), and basal conditions (Leysinger-Vieli et al., 2018; Wolovick et al., 2014).

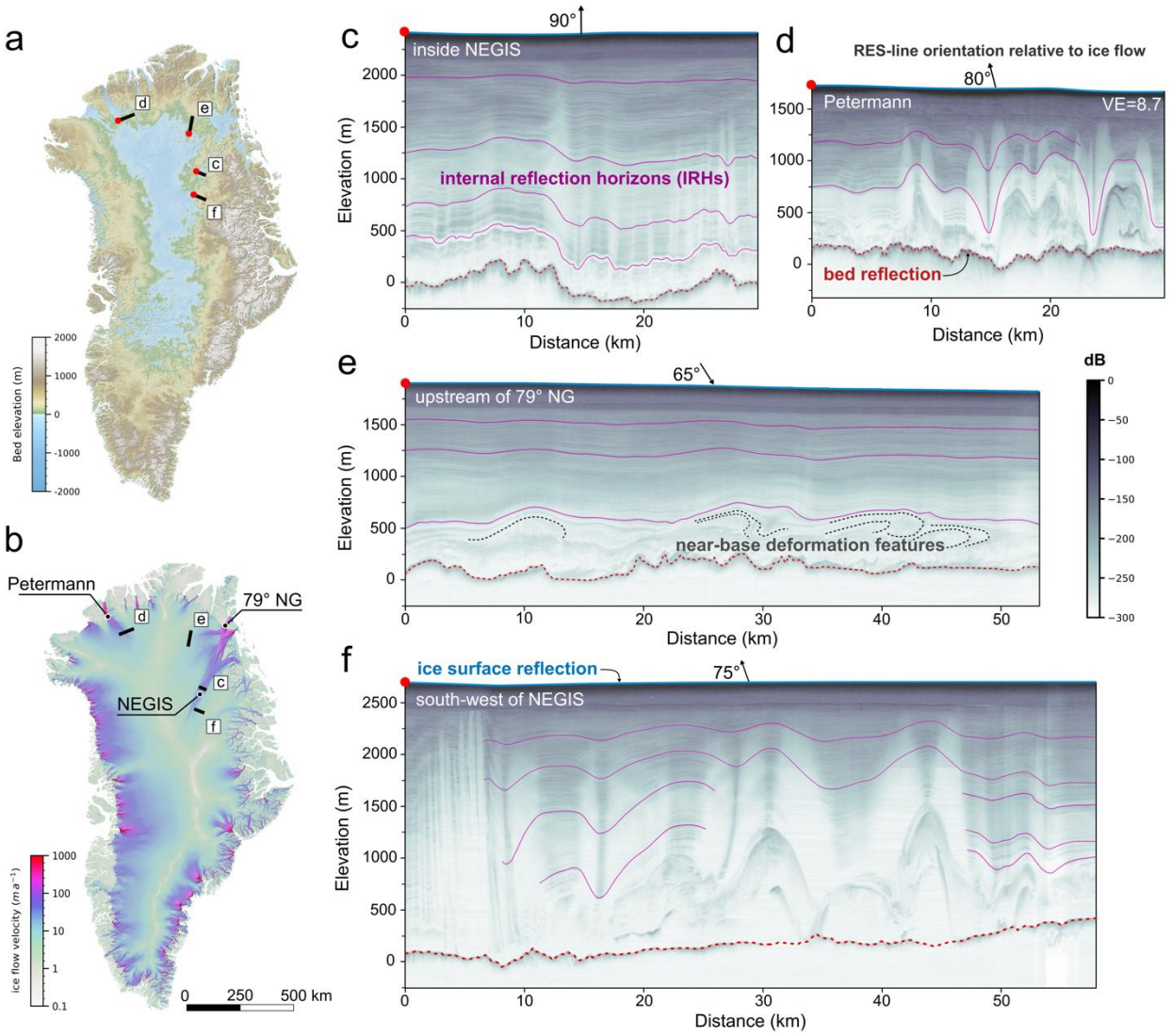

Figure 1. Overview of the Greenland ice sheet and radio-echo sounding (RES) profiles: (a) bed topography (Morlighem et al., 2017) and location of RES profiles; (b) ice surface flow velocity (Joughin et al., 2018); (c-f) RES images showing englacial folds (c) in the central North-East Greenland Ice Stream (NEGIS), (d) at the Petermann ice stream, (e) upstream of the 79° North Glacier (Nioghalvfjerdsbrae), and (f) in the upstream region of the NEGIS. Note the strong vertical exaggeration (8.7) in RES-profiles. Arrows show the average flow direction relative to the profiles.

Several mechanisms and models have been proposed to explain the formation of folds in the ice sheet. Bell et al. (2014) and Leysinger-Vieli et al. (2018) suggest that refreezing meltwater adds material to the ice base and elevates the overlying stratigraphy and influences basal ice deformation. Alternatively, Wolovick et al. (2014) suggest that variable slip rates due to "basal slippery patches" can create large-scale folds. Furthermore, Krabbendam (2016) proposes the basal temperate (melting) ice layer may be locally thickened by internal deformation of folding or thrusting over a bedrock high. The above mentioned variable basal resistance or basal freeze-on/melting models all require special or complex basal ice and bedrock conditions, which

seems at odds with the presence of folds throughout the GrIS. Additionally, all these concepts use single RES sections and implicitly assume that the fold axis orientation is at a high angle to the direction of ice flow. However, the three-dimensional geometry of folds show that folds are rather parallel or at a small angle to the flow direction (Bons et al., 2016; Franke et al., 2022a, 2023).

Hudleston (2015) proposes that irregularities in primary ice stratification can be kinematically amplified in convergent flow by horizontal shortening and without the requirement of rheological contrast in the ice. Bons et al. (2016) suggest that mechanical anisotropy and convergent flow cause large-scale folding in Greenland's ice sheet. However, the question which factors actually contribute to folding, or why initial irregularities of ice layers would be amplified, is still unclear. Moreover, there is a need for more and better numerical modeling to trace the widespread deformation of internal ice layers.

Three properties of ice or ice sheets are significant for the modeling of flow in ice sheets: (1) The viscoplastic deformation of the ice I_h (hexagonal ice) results essentially from dislocation glide parallel to the crystallographic basal plane (Gillet-Chaulet et al., 2006). The crystallographic preferred orientation (CPO) in ice sheets is typically a vertical alignment of the crystals' c-axes, which are perpendicular to the easy-glide basal planes. As a result, the ice becomes significantly anisotropic in its flow properties (Duval et al., 1983; Llorens et al., 2017). (2) Due to geothermal heat flux (Artemieva, 2019), ice temperature increases with depth: upper "cold ice" has a high viscosity and density, while the lower "warm ice" has a lower viscosity and also has a low density due to thermal expansion (Hills et al., 2017; Krabbendam, 2016). (3) Ice layers are initially not necessarily perfect sheets with constant thickness, and variations in thickness may form due to the underlying bedrock topography (Hudleston, 2015). Taking these considerations into account, we here use numerical modeling to investigate the development of folds in 3D convergent flow. We particularly investigate the factors of rheological anisotropy of ice, vertical viscosity and density contrasts, and bedrock conditions.

2 Method

2.1 Full-Stokes Code Underworld2

We used the Full-Stokes software "Underworld 2" (Beucher et al., 2022). The code was originally designed and developed for modeling and tracking internal deformation in geodynamic processes and is therefore specifically optimized for our case. Some of the advantages are (i) tracking of material "particles" during deformation and (ii) local fabric evolution can be coupled to the local rheological anisotropy.

Underworld 2 uses the material point method (MPM), which is related to the better-known particle-in-cell method (Moresi et al., 2003). MPM uses an Eulerian finite-element mesh to calculate the incremental development of the velocity field and other field variables, such as temperature and pressure, while Lagrangian material points ("particles") carry the density, viscosity, lattice orientation, and other relevant local material parameters. This code is already well established in complex geodynamic modeling with a full-Stokes solution for isotropic and anisotropic elasto–visco–plastic materials (Moresi & Mühlhaus, 2006; Sharples et al., 2016). The software has also passed the usual benchmark tests for full-Stokes ice sheet models of Pattyn et al. (2008) (Sachau et al., 2022).

115 2.2 Physics

116 In our model, the temperature (T, ℃) is -30 ℃ (T_0) for cold ice and, below a height
117 $h_{warmice}$, in what is here termed "warm ice", the temperature increases downward to -3 ℃ (T_{bed}) at
118 the base (Hills et al., 2017; Rogozhina et al., 2011) with a parabolic equation:

119 $$T = T_{bed} + (T_0 - \mathrm{T_{bed}})\left(\frac{y - h_{bed}}{h_{warmice} - h_{bed}}\right)^{1.2} \quad (1)$$

120 where y is the height in warm ice, and h_{bed} and $h_{warmice}$ are the heights for bedrock surface and
121 warm ice surface.

122 The ice density (ρ, $\mathrm{kg/m^3}$) is given as a function of temperature by:

123 $$\rho = \frac{1.802\times10^4}{19.30447 - 7.988471\times10^{-4}\cdot(T+273) + 7.563261\times10^{-6}\cdot(T+273)^2}. \quad (2)$$

124 Equation (2) is derived from the molar volume equation for pure ice at 1 atm in Marion and
125 Jakubowski (2004), where the molar mass of H_2O is assumed to be 1.802×10^4 kg/mol.

126 The non-linear viscous ice flow is based on Kuiper's flow law for dislocation creep
127 (Kuiper et al., 2020), an advanced version from Glen (1955) and Goldsby (2006), where the
128 strain rate ($\dot{\varepsilon}_{ij}$) is proportional to the deviatoric stress (τ_{ij}) to the power n,

129 $$\dot{\varepsilon}_{ij} = A_0 \mathrm{e}^{\frac{-Q}{R(T+273)}} \tau_{II}^{\mathrm{n-1}} \tau_{ij} \quad (3)$$

130 where A_0 is the material parameter, Q the activation energy, R the gas constant and τ_{II} the
131 second invariant of the deviatoric stress tensor τ_{ij}, and the stress exponent n is 4 for polar ice
132 sheets (Bons et al., 2018). The power-law viscosity of ice (isotropic viscosity η_1, Pa · s) is
133 derived from temperature and strain rate (Sachau et al., 2022)

134 $$\eta_1 = \frac{1}{2}\left(A_0 \mathrm{e}^{\frac{-Q}{R(T+273)}}\right)^{\frac{-1}{n}} \cdot \dot{\varepsilon}_{II}^{\frac{1-n}{n}} \cdot 10^6 \quad (4)$$

135 where $\dot{\varepsilon}_{II}$ is the second invariant of the strain rate tensor.

136 The c-axis orientation of the ice crystal is stored for each particle in Underworld2. Initial
137 c-axis directions of ice particles are perpendicular to the local layer orientation with a Gaussian
138 random distribution with a standard deviation of ±5°. As the simulation progresses, the c-axes
139 rotate in the flow field according to the symmetric deformation-rate tensor D and the skew-
140 symmetric rotation-rate tensor W

141 $$D = \frac{1}{2}(L + L^{\mathrm{T}}) \quad (5)$$

142 $$W = \frac{1}{2}(L - L^{\mathrm{T}}) \quad (6)$$

143 where L is the velocity gradient tensor (see Appendix B in Sharples et al. (2016) for detailed
144 rotation equations).

145 The anisotropy of the ice crystal is modeled as transverse isotropy, which is a common
146 practice in numerical modeling (Gillet-Chaulet et al., 2005; Martín et al., 2009; Sharples et al.,
147 2016). Transverse isotropic viscosity is defined by two viscosity values: a general viscosity η_1
148 (Pa · s) and a second viscosity η_2 (Pa · s) perpendicular to the c-axis direction. η_1 is set
149 proportional to η_2:

$$\eta_1 = k\eta_2 \quad (7)$$

where k represents the rheological anisotropy value. If the stress exponent n is 3 and given the same strain rate, the stress required for non-basal deformation of ice monocrystals is at least 60 times higher than for basal slip (Llorens et al., 2017). For macroscopic ice polycrystals, the ratio is about ten (Duval et al., 1983). For the assumed $n = 4$ in our macroscopic ice model, k is approximately six. However, $k = 6$ requires a high grid resolution to avoid numerical instabilities that may lead to artificial amplification of small folds. For this reason we employed a smaller $k = 3$, which thus underestimates the expected anisotropy in the ice. We will show that the main factor controling folding is not the k-value once significantly larger than unity, but whether the ice is anisotropic or not.

2.3 Model Design

The basic design is shown in Figures 2a-2d (detailed parameters in Table S1 and Figure S1 in Supporting Information SI). It consists of four main sets of layers: air (500 m), cold ice (1667 m), warm ice (833 m) and bedrock, and 10 internal marker horizons to track the deformation. Three different bedrock conditions are tested: (i) free-slip bottom boundary without a bedrock (Figure 2b), (ii) a 1000 m thick bedrock layer with a flat surface to which the ice is frozen (Figure 2c), and (iii) the same as (ii), but with an undulating bedrock surface with bumps of variable wavelengths and amplitudes (Figure 2d). Internal horizons adapt to bedrock bumps, where basal ice layers have larger initial amplitudes, which we refer to as 'noise' in this article. The ‘initial noise’ gradually decreases from the ice-bedrock interface to zero at the ice surface. Internal horizons are progressively shortened from the right (negative Z-axis direction) by a lateral inflow at 5 $\mathrm{m/yr}$, at the right boundary. The horizontal velocity is set to zero at the left boundary. To reduce computing time, the model thus consist of one half of a convergent zone, as for example envisaged by Bons et al. (2016) for the inlet area of the Petermann Glacier. Simultaneously, there is outflow in the third dimension (positive X-axis; Figure 2a), which compensates the inflow and thus maintains a constant ice volume.

Six models are discussed here for the impact of ice properties (anisotropy, visosity and density) and bedrock conditions on large-scale folding. In these models we varied the following parameters: (1) bedrock condition (i) for Models 1-2, bedrock condition (ii) for Model 3, and bedrock condition (iii) (variable amplitude bumps up to 400 m) for Models 4-5; (2) isotropic ice for Model 1 and Model 5, and anisotropic ice for all other models (see detailed comparison of all models in Table S2 in Supporting Information SI).

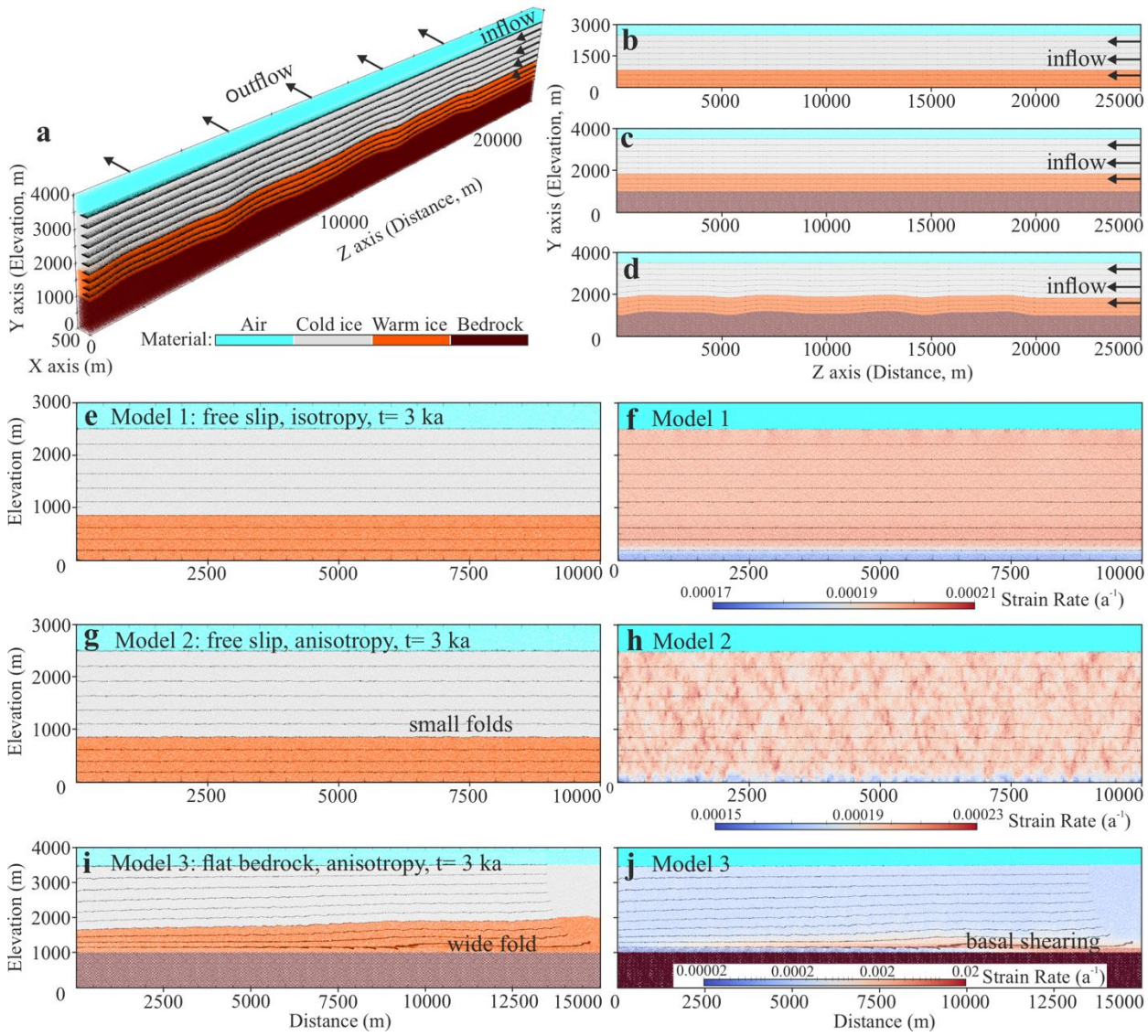

Figure 2. Model design and snapshots of results from Models 1-3 after 3000 years: (a) 3D view of initial model (example from bumpy bedrock model); (b-d) profiles parallel to Z-Y coordinate plane showing three bedrock types (b) free-slip bottom boundary, (c) flat bedrock surface and (d) bumpy bedrock surface; (e-l) results of material map and the second invariant of strain-rate magnitude for (e-f) Model 1, (g-h) Model 2 and (i-j) Model 3.

3 Results

3.1 Effect of Anisotropy, Viscosity and Density

In the simulations of isotropic ice on a free-slip bottom boundary (Model 1), ice layers stay nearly flat for at least 3000 years, even with both vertical viscosity and density contrasts (Figures 2e-2f). Nevertheless, when anisotropy is included in the models, a large number of small folds (less than 40 m fold amplitude) form (Model 2; Figures 2g-2h), due to the Gaussian variability of the c-axis orientation of particles. Compared to the very homogeneous strain rates

resulting from the isotropic Model 1 (Figure 2f), the strain-rate map of Model 2 is much more heterogeneous with clusters of high strain rates (Figure 2h).

3.2 Effect of Bedrock Topography

In the scenario where bedrock is added as a horizontal flat layer underneath the anisotropic ice (Model 3; Figure 2i) shearing occurs to the basal ice layers as the ice is frozen to the bedrock. The slip resistance at the bedrock interface results in thickening of the ice at the inflow side, which shows as the development of a wide fold (up to 140 m amplitude). Abundant small folds appear with amplitudes that range up to 80 m around this wide fold. The strain-rate field (Figure 2j) shows a horizontal band of high strain rates along this wide fold. Strain rates decrease in upper ice layers but are still higher than in Model 2. For the scenario with a bumpy bedrock topography (Model 4), the initial ice layers on bedrock bumps start to evolve into large-scale folds (larger than 200 m amplitude after 3000 years) and additional small folds in between (Figures 3a-3e).

3.3 Anisotropic vs. isotropic ice on the bumpy bedrock

We explore the effect of anisotropic (Model 4) and isotropic ice (Model 5) on a bumpy bedrock in a 3000-year-long simulation (Figure 3). Here we compare three large-scale fold sets A, B, and C (Figure 3), in terms of the fold amplitudes as a function of layer height. Amplitude is here defined as the difference in elevation of a marker horizon at a fold crest and adjacent trough. The height is defined as the average of crest and trough elevation. We consider 10 stratigraphic layers labeled 1-10 from bottom to top (Figure 3a). The amplitude-height values of Layers 3-10 are shown in Figure S4 in Supporting Information SI (note that Layers 1-2 are too close to the bedrock and therefore strongly sheared). In Model 4, the amplitude of the initial layer noise is largest in the near-base layers and zero at the ice surface. The largest fold amplitudes are in middle layers (Layers 4-6) and mostly exceed the initial layer noise. In the isotropic Model 5 we observe large-scale folds that are inherited from the initial noise. They are smaller and smoother, and without small folds in between (Figures 3f-3i). Folds with the largest amplitudes are found in the deepest layers, and amplitudes of most folds are smaller than the initial noise. Strain rates in Model 5 are high close to the ice base, decrease towards the ice surface in the upper layers and are distributed in a regular pattern associated with bedrock bumps (Figure 3i).

The only difference in the settings between Model 4 and Model 5 is the anisotropy in the ice. Since the fold growth of fold sets A, B and C is greater in the anisotropy case, we define the "amplified amplitude by anisotropy" by subtracting the fold amplitude of the isotropy model (Model 5) from that of the anisotropy model (Model 4). After 3000 years (Figure 3j), the amplified amplitudes by anisotropy of most folded layers are larger than 0 m, indicating that anisotropy does amplify folds after this period. The maximum amplification of over 100 m is in the middle layers (Layers 5-7).

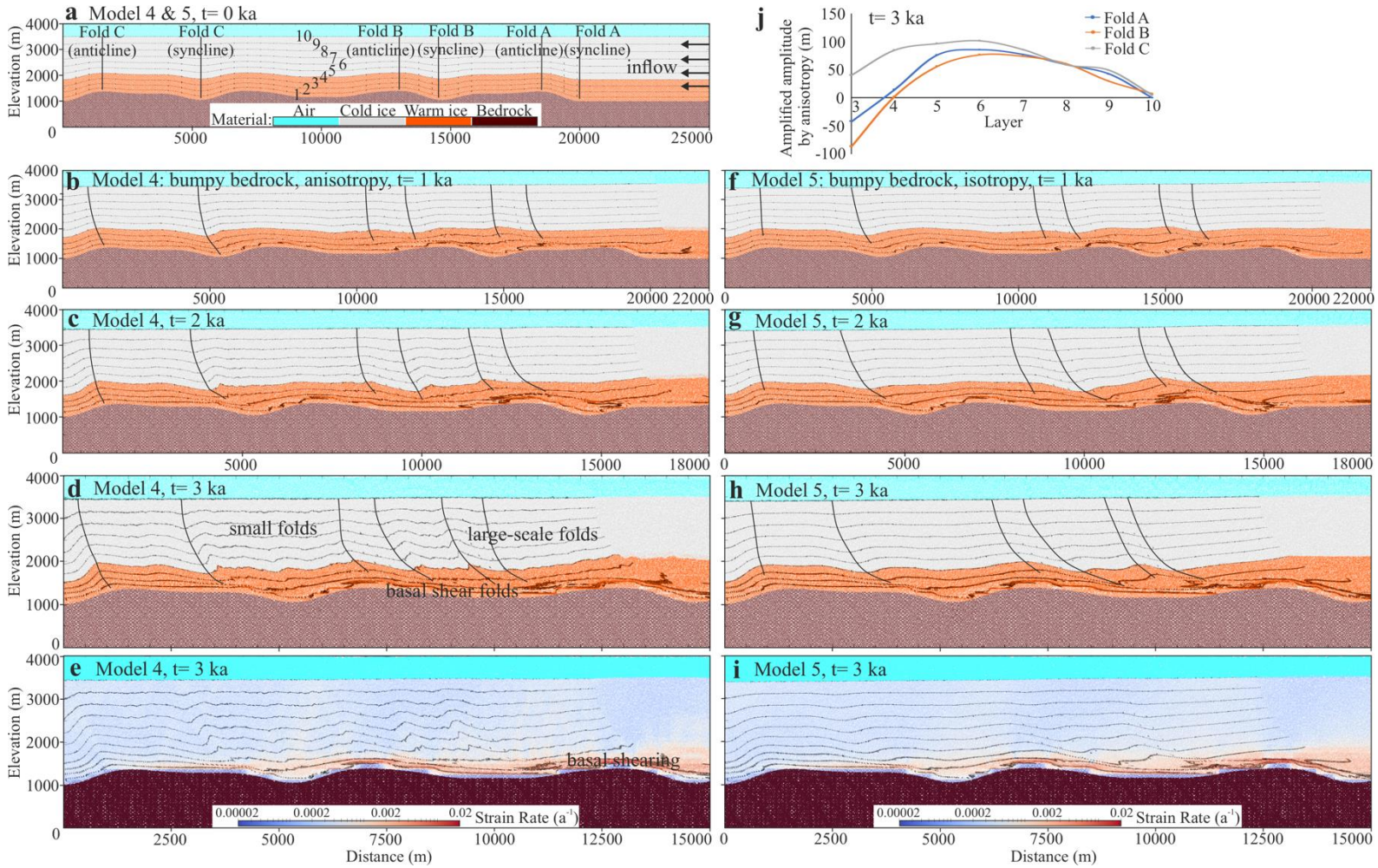

Figure 3. Snapshots of comparison of anisotropic Model 4 and isotropic Model 5 with an identical bedrock topography with 400 m tall bumps in both models shown in (a): (b-d) Layer geometry snapshots of Model 4 after (b) 1000 years, (c) 2000 years and (d) 3000 years. (e) The second invariant of strain-rate magnitude in Model 4 at 3000 years. (f-h) Layer geometry snapshots of Model 5 after 1000, 2000 and 3000 years. (i) The second invariant of strain-rate magnitude for Model 5 after 3000 years. Note that the z-axis and y-axis scales between the images of individual time steps. (j) Amplified amplitudes by anisotropy of Layers 3-10 on Fold A, Fold B and Fold C after 3000 years.

4 Discussion

4.1 Controlling factors for fold growth

The folds observed in our modeling can be classified into three types: large-scale folds (fold amplitudes >100 m), small-scale folds (fold amplitudes <<100 m, wavelength <<km) and basal shear folds (recumbent folds). The large-scale folds have wavelengths in the order of a km or more. Their axial planes have a listric shape, with steep dips near the ice surface that become shallower towards the bedrock. Our simulated large-scale folds (in particular those in Model 4) show strong similarity to those observed in Greenland's ice sheet by e.g., MacGregor et al. (2015), Bons et al. (2016) and Franke et al. (2022a) (Figure 1).

The main controlling factors for large-scale folds in our simulations are ice anisotropy and the initial geometry dictated by the underlying bedrock topography. Folds in isotropic ice (k=1) (Figures 3f-3i) are essentially palimpsests of the underlying bedrock topography that are passively transported away from the underlying bumps. They do not amplify by themsleves, but passively change their shape as they travel over bedrock bumps. In the anisotropic model with k=3 (Figures 3b-3e), we observed additional fold-shape modification and amplification. When k is set to 6 (Figure S5 in Supporting Information SI) this effect is even stronger. This is a clear indication that the anisotropy plays a primary role in fold amplification. However, we also observe that fold amplitudes increase with increasing bedrock topography, as can be seen in Figures 3b-3e, and S6-S7 (in Supporting Information SI) with the highest bedrock topography amplitude of 600 m.

According to classical fold theory (Biot, 1957; Schmalholz and Mancktelow, 2016) folds form by the amplification of small perturbations in the folding layer. In case of folding of a strong layer in a softer matrix, a dominant wavelength will develop as a function of layer thickness (the characteristic length scale of the system) and the viscosity ratio of the layer and matrix. The dominant wavelength is the wavelength with the highest amplification rate. In case of a single, but anisotropic medium, a characteristic length scale is absent. As a consequence there is no dominant wavelength that amplifies the most, and folds of all wavelengths may form simulataneously, including small-scale folds (Figure 2g). Bedrock topography creates seed folds with significant amplitudes. With these, the system can "skip" the initial fold nucleation for folds with these wavelengths. Depending on the intensity of the anisotropy (k) these folds will amplify. However, in case of anisotropy small-scale folds will also nucleate due to small-scale perturbations (here the random noise in c-axis orientations).

In our models, the lowermost ice is warmer, which creates a system with a cold and strong layer at the top and a warmer and softer layer at the bottom. At the top the cold ice is in contact with air, which has an almost infinitely lower viscosity compared to ice. Shortening of this layer system could potentially lead to buckle folding, as has been suggested by the NEEM-community (2013). Initial wavelengths for low viscosity contrasts would be at least five to ten times the layer thickness (Llorens et al., 2013; Schmalholz and Mancktelow, 2016), which in our case would be at least 5 to 10 km. However, the dominant wavelength due to the ice-air interface with an almost infinite viscosity contrast would by far exceed the width of the model, and even

that of an ice sheet. The viscosity contrast between the warm and cold ice is relatively low and lacks a sharp boundary. Although the resulting wavelengths are in the same order as of folds observed in the ice sheets, the amplification rate is very small (Llorens et al., 2013) and no visible folds can form. These theoretical considerations, as well as the results of models 1 and 3 (isotropy, no bedrock bumps), indicate that Biot-type buckle folding due to viscosity contrasts between cold ice and air above and warm ice below cannot lead to significant folding on the multi-km scale.

Deformation in the deepest, softest ice is approximately in simple shear. In case of bedrock bumps, the basal shear zone may localise above the bedrock-ice interface, especially across throughs in the bedrock (Figure 3e). This effect is more pronounced in case of anisotropy (Sachau et al., 2022). Passive shearing of layers in heterogneous simple shear leads to tight recombant folds (Figures 3d and 3h) that are also observed in ice sheets (Figure 1e; Bons et al., 2016). Recumant folding may be enhanced by anisotropy, but is largely controled by the deep bedrock-parallel shearing and bedrock topography, not by anisotropy. Connection of the deep recumbant folds with a shallowly dipping axial plane with more upright folds higher up in the ice leads to the listric shape of the axial planes (Franke et al., 2022a).

4.2 A generic mode for large-scale folding

Tracking the kinematic processes of ice layers, the formation of large-scale folding can be summarized in three stages: (1) Irregularities in primary ice stratification result mainly from undulating bedrock topography and become initial seeds for subsequent large-scale folding. (2) As lateral convergence continues, anisotropy comes into play and initial noise in the internal horizons is amplified. Internal ice horizons deform especially at both sides of a bedrock bump, but not on the summit of the bump where the ice above the basal shear zone can slide without further folding (Figure 3e). Meanwhile, anisotropy does also lead to smaller-scale folds that result from the amplification of noise in the system. The constraint of the bedrock has a significant impact on the deepest stratigraphic horizons, which can shear, rotate and develop complex structural patterns. (3) Finally, initial noise evolves into larger-scale folds and internal horizons in the middle of the ice column are amplified the most (not necessarily at the interface of warm and cold ice).

We should notice that our model may not yet well explain some extremely tall plume-like folds (e.g. over 800 m fold amplitude in Figure 1d). Our model is at a starting point of the large-scale folding formation. However, these folds are probably much older and can undergo multi-stage deformations during the long evolution of the ice sheet. Due to the density contrasts with cold ice above, the buoyancy of the warm ice below may also contribute to amlification of large-scale folds over long time scales. Our model size could be another limitation. The maximum strain is about 50% shortening in our bumpy bedrock models (e.g. Figures 3a-3e). The folds could be amplified more with an increasing strain but that would require a much larger model size (more computing time) to obtain a suitable fold wavelength. These problems are expected to be carefully tested and improved in future modeling.

5 Conclusions

Motivated by observations of folds in radargrams of the Greenland ice sheet, we conducted full-Stokes ice flow modeling with Underworld2 to reproduce large-scale englacial folds. Our modeling results show that: (1) Large-scale folds can form in convergent ice flow and are mainly controlled by rheological anisotropy of ice and bedrock topography, instead of vertical viscosity contrasts from temperature gradients in ice layers. (2) As observed in ice sheets, large-scale fold amplitudes are highest in the middle of the ice column and decrease towards the surface. Meanwhile, near-base fold patterns are more complex and often result in recumbent folds due to the bedrock constraint. (3) Ice anisotropy due to the CPO allows to produce small-scale folds on initially flat internal horizons. Finally, using movement tracking and strain analysis, our modeling helps to better understand ice-flow dynamics of the Greenland ice sheet. In particular, an improved implementation of ice anisotropy and basal shearing can result in high-strain-rate areas where the power-law ice would be softened, even on a frozen ground. This indicates that ice sheets could be more unstable when suddenly triggered to flow by external forcings, such as climate change, ice-sheet geometry changes or tectonic events.

Acknowledgments

Steven Franke was funded by the Walter Benjamin Programme of the German Research Foundation (Deutsche Forschungsgemeinschaft; DFG) – project number: 506043073, and Yu Zhang by the China Scholarship Council (grant no. 202006010063).

Open Research

Underworld is fully open-source and the version (v2.14.1b) used for this paper is available through Mansour et al. (2022) https://doi.org/10.5281/zenodo.5935717. Our code files for all the models are available through Zenodo https://doi.org/10.5281/zenodo.10265944. The radio-echo sounding data shown in Figure 1c (profile IDs: 20180509_01_[011, 012]) and in Figure 1f (profile ID: 20180512_02_009) from AWI's EGRIP-NOR-2018 survey are available under https://doi.org/10.1594/PANGAEA.928569 (Franke et al., 2022b), the data shown in Figure 1d (profile ID: 20110507_01_032) is available via the CReSIS Data Products (https://data.cresis.ku.edu/) and the data shown in Figure 1e (profile ID: 20180415_06_007) is available under https://doi.org/10.1594/PANGAEA.949391 (Franke et al., 2022a). Bed elevation data from Morlighem et al. (2017) and ice flow velocity data from Joughin et al. (2018) are

available at the National Snow and Ice Data Center: https://nsidc.org/data/idbmg4 and https://nsidc.org/data/nsidc-0670/, respectively.

References

Artemieva, I. M. (2019). Lithosphere thermal thickness and geothermal heat flux in Greenland from a new thermal isostasy method. *Earth-Science Reviews*, 188, 469-481. https://doi.org/10.1016/j.earscirev.2018.10.015

Bell, R. E., Tinto, K., Das, I., Wolovick, M., Chu, W., Creyts, T. T., et al. (2014). Deformation, warming and softening of Greenland's ice by refreezing meltwater. *Nature Geoscience*, 7(7), 497-502. https://doi.org/10.1038/ngeo2179

Beucher, R., Giordani, J., Moresi, L., Mansour, J., Kaluza, O., Velic, M., et al. (2022). Underworld2: Python Geodynamics Modelling for Desktop, HPC and Cloud (v2.14.1b) [Software]. Zenodo. https://doi.org/10.5281/zenodo.7455999

Biot, M. A. (1957). Folding instability of a layered viscoelastic medium under compression. *Proceedings of the Royal Society of London. Series A. Mathematical and Physical Sciences*, 242(1231), 444-454. https://doi.org/10.1098/rspa.1957.0187

Bons, P. D., Jansen, D., Mundel, F., Bauer, C. C., Binder, T., Eisen, O., et al. (2016). Converging flow and anisotropy cause large-scale folding in Greenland's ice sheet. *Nature communications*, 7(1), 11427. https://doi.org/10.1038/ncomms11427

Bons, P. D., Kleiner, T., Llorens, M. G., Prior, D. J., Sachau, T., Weikusat, I., & Jansen, D. (2018). Greenland Ice Sheet: Higher nonlinearity of ice flow significantly reduces estimated basal motion. *Geophysical Research Letters*, 45(13), 6542-6548. https://doi.org/10.1029/2018GL078356

373 Duval, P., Ashby, M. F., & Anderman, I. (1983). Rate-controlling processes in the creep of
374 polycrystalline ice. *The Journal of Physical Chemistry*, 87(21), 4066-4074.
375 https://doi.org/10.1021/j100244a014
376 Franke, S., Bons, P. D., Westhoff, J., Weikusat, I., Binder, T., Streng, K., et al. (2022a).
377 Holocene ice-stream shutdown and drainage basin reconfiguration in northeast Greenland.
378 *Nature Geoscience*, 15(12), 995-1001. https://doi.org/10.1038/s41561-022-01082-2
379 Franke, S., Jansen, D., Binder, T., Paden, J. D., Dörr, N., Gerber, T. A., et al. (2022b). Airborne
380 ultra-wideband radar sounding over the shear margins and along flow lines at the onset region of
381 the Northeast Greenland Ice Stream. *Earth System Science Data*, *14*(2), 763–779.
382 https://doi.org/10.5194/essd-14-763-2022
383 Franke, S., Bons, P. D., Streng, K., Mundel, F., Binder, T., Weikusat, I., et al. (2023). Three-
384 dimensional topology dataset of folded radar stratigraphy in northern Greenland. *Scientific Data*,
385 *10*(1), 525. https://doi.org/10.1038/s41597-023-02339-0
386 Gillet-Chaulet, F., Gagliardini, O., Meyssonnier, J., Montagnat, M., & Castelnau, O. (2005). A
387 user-friendly anisotropic flow law for ice-sheet modeling. *Journal of Glaciology*, 51(172), 3-14.
388 https://doi.org/10.3189/172756505781829584
389 Gillet-Chaulet, F., Gagliardini, O., Meyssonnier, J., Zwinger, T., & Ruokolainen, J. (2006).
390 Flow-induced anisotropy in polar ice and related ice-sheet flow modelling. *Journal of non-*
391 *newtonian fluid mechanics*, 134(1-3), 33-43. https://doi.org/10.1016/j.jnnfm.2005.11.005
392 Glen, J. W. (1955). The creep of polycrystalline ice. Proceedings of the Royal Society of
393 London. Series A. *Mathematical and Physical Sciences*, 228(1175), 519-538.
394 https://doi.org/10.1098/rspa.1955.0066

Goldsby, D. L. (2006). Superplastic flow of ice relevant to glacier and ice-sheet mechanics. *Glacier science and environmental change*, 308-314. https://doi.org/10.1002/9780470750636.ch60

Hills, B. H., Harper, J. T., Humphrey, N. F., & Meierbachtol, T. W. (2017). Measured horizontal temperature gradients constrain heat transfer mechanisms in Greenland ice. *Geophysical Research Letters*, 44(19), 9778-9785. https://doi.org/10.1002/2017GL074917

Hudleston, P. J. (2015). Structures and fabrics in glacial ice: A review. *Journal of Structural Geology*, 81, 1-27. https://doi.org/10.1016/j.jsg.2015.09.003

Joughin, I. A. N., Smith, B. E., & Howat, I. M. (2018). A complete map of Greenland ice velocity derived from satellite data collected over 20 years. *Journal of Glaciology*, 64(243), 1-11. https://doi.org/10.1017/jog.2017.73

Krabbendam, M. (2016). Sliding of temperate basal ice on a rough, hard bed: creep mechanisms, pressure melting, and implications for ice streaming. *The Cryosphere*, 10(5), 1915-1932. https://doi.org/10.5194/tc-10-1915-2016

Kuiper, E. J. N., De Bresser, J. H., Drury, M. R., Eichler, J., Pennock, G. M., & Weikusat, I. (2020). Using a composite flow law to model deformation in the NEEM deep ice core, Greenland–Part 2: The role of grain size and premelting on ice deformation at high homologous temperature. *The Cryosphere*, 14(7), 2449-2467. https://doi.org/10.5194/tc-14-2449-2020

Leysinger Vieli, G. M., Martin, C., Hindmarsh, R. C. A., & Lüthi, M. P. (2018). Basal freeze-on generates complex ice-sheet stratigraphy. *Nature Communications*, 9(1), 4669. https://doi.org/10.1038/s41467-018-07083-3

Llorens, M. G., Bons, P. D., Griera, A., Gomez-Rivas, E., & Evans, L. A. (2013). Single layer folding in simple shear. *Journal of Structural Geology*, 50, 209-220. https://doi.org/10.1016/j.jsg.2012.04.002

Llorens, M. G., Griera, A., Steinbach, F., Bons, P. D., Gomez-Rivas, E., Jansen, D., et al. (2017). Dynamic recrystallization during deformation of polycrystalline ice: insights from numerical simulations. *Philosophical Transactions of the Royal Society A: Mathematical, Physical and Engineering Sciences*, 375(2086), 20150346. https://doi.org/10.1098/rsta.2015.0346

MacGregor, J. A., Fahnestock, M. A., Catania, G. A., Paden, J. D., Prasad Gogineni, S., Young, S. K., et al. (2015). Radiostratigraphy and age structure of the Greenland Ice Sheet. *Journal of Geophysical Research: Earth Surface*, 120(2), 212-241. https://doi.org/10.1002/2014JF003215

Marion, G. M., & Jakubowski, S. D. (2004). The compressibility of ice to 2.0 kbar. *Cold Regions Science and Technology*, 38(2-3), 211-218. https://doi.org/10.1016/j.coldregions.2003.10.008

Martín, C., Gudmundsson, G. H., Pritchard, H. D., & Gagliardini, O. (2009). On the effects of anisotropic rheology on ice flow, internal structure, and the age-depth relationship at ice divides. *Journal of Geophysical Research: Earth Surface*, 114(F4). https://doi.org/10.1029/2008JF001204

Moresi, L., & Mühlhaus, H. B. (2006). Anisotropic viscous models of large-deformation Mohr–Coulomb failure. *Philosophical Magazine*, 86(21-22), 3287-3305. https://doi.org/10.1080/14786430500255419

Moresi, L., Dufour, F., & Mühlhaus, H. B. (2003). A Lagrangian integration point finite element method for large deformation modeling of viscoelastic geomaterials. *Journal of computational physics*, 184(2), 476-497. https://doi.org/10.1016/S0021-9991(02)00031-1

Morlighem, M., Williams, C. N., Rignot, E., An, L., Arndt, J. E., Bamber, J. L., ... & Zinglersen, K. B. (2017). BedMachine v3: Complete bed topography and ocean bathymetry mapping of Greenland from multibeam echo sounding combined with mass conservation. *Geophysical research letters*, 44(21), 11-051. https://doi.org/10.1002/2017GL074954

NEEM community members. (2013). Eemian interglacial reconstructed from a Greenland folded ice core. *Nature*, 493, 489–494. https://doi.org/10.1038/nature11789

Pattyn, F., Perichon, L., Aschwanden, A., Breuer, B., De Smedt, B., Gagliardini, O., ... & Zwinger, T. (2008). Benchmark experiments for higher-order and full-Stokes ice sheet models (ISMIP–HOM). *The Cryosphere*, 2(2), 95-108. https://doi.org/10.5194/tc-2-95-2008

Rogozhina, I., Martinec, Z., Hagedoorn, J. M., Thomas, M., & Fleming, K. (2011). On the long-term memory of the Greenland Ice Sheet. *Journal of Geophysical Research: Earth Surface*, 116(F1). https://doi.org/10.1029/2010JF001787

Sachau, T., Yang, H., Lang, J., Bons, P. D., & Moresi, L. (2022). ISMIP-HOM benchmark experiments using Underworld. *Geoscientific Model Development*, 15(23), 8749-8764. https://doi.org/10.5194/gmd-15-8749-2022

Schmalholz, S. M., & Mancktelow, N. S. (2016). Folding and necking across the scales: a review of theoretical and experimental results and their applications. *Solid Earth*, 7(5), 1417-1465. https://doi.org/10.5194/se-7-1417-2016

Sharples, W., Moresi, L. N., Velic, M., Jadamec, M. A., & May, D. A. (2016). Simulating faults and plate boundaries with a transversely isotropic plasticity model. *Physics of the Earth and Planetary Interiors*, 252, 77-90. https://doi.org/10.1016/j.pepi.2015.11.007

Wolovick, M. J., Creyts, T. T., Buck, W. R., & Bell, R. E. (2014). Traveling slippery patches produce thickness-scale folds in ice sheets. *Geophysical Research Letters*, 41(24), 8895-8901. https://doi.org/10.1002/2014GL062248

Reference From the Supporting Information

Pettit, E. C., Waddington, E. D., Harrison, W. D., Thorsteinsson, T., Elsberg, D., Morack, J., & Zumberge, M. A. (2011). The crossover stress, anisotropy and the ice flow law at Siple Dome, West Antarctica. *Journal of Glaciology*, 57(201), 39-52. https://doi.org/10.3189/002214311795306619